J. Fluid Mech. (1981), *vol.* 112, *pp.* 379–396
Printed in Great Britain

Taylor hypothesis and large-scale coherent structures

By K. B. M. Q. ZAMAN AND A. K. M. F. HUSSAIN
Department of Mechanical Engineering, University of Houston, Texas 77004

(Received 26 June 1980 and in revised form 8 December 1980)

The applicability of the Taylor hypothesis to large-scale coherent structures in turbulent shear flows has been evaluated by comparing the *actual* spatial distributions of the structure properties with those deduced through the use of the hypothesis. This study has been carried out in the near field of a 7·62 cm circular air jet at a jet Reynolds number of $3{\cdot}2 \times 10^4$, where the coherent structures and their interactions have been organized through controlled excitation. Actual distributions of the structure properties have been obtained through phase-average hot-wire data, the measurements having been repeated at different spatial points over the extents of the structure cross-sections at a fixed phase. The corresponding 'spatial' distributions of these properties obtained (by using the Taylor hypothesis) from the temporal data at appropriate phases and locations, show that the hypothesis works quite well for an isolated coherent structure if a constant convection velocity, equal to the structure centre velocity, is used in the hypothesis everywhere across the shear flow. The popular use of the local time-average or even the instantaneous streamwise velocity produces unacceptably large distortions. When structure interactions like pairing are involved, no convection velocity can be found with which the hypothesis works. Distributions of the terms in the Navier–Stokes equation contributing to the phase-average vorticity, but neglected by the hypothesis, have been quantitatively determined. These show that the terms associated with the background turbulence field, but not those associated with the coherent motion field, can be neglected. In particular, the pressure term due to the coherent motion field is large and cannot be neglected.

1. Introduction

In turbulent flows, a spatial description of the flow structure is of primary interest. However, economy, convenience and inherent constraints dictate use of a limited few sensors which typically provide time-traces of flow variables at stationary locations. The researcher thus has had to endeavour to deduce spatial descriptions from temporal information recorded by stationary sensors. Taylor (1938) hypothesized that the time-history of the flow signal from a stationary probe can be regarded as that due to advection of a 'frozen' spatial pattern of turbulence past the probe with the mean speed U, i.e. $u(x,t) = u(x-Ut,0)$, and Favre, Gaviglio & Dumas (1952) were the first to demonstrate experimentally its validity for grid turbulence. This 'Taylor hypothesis' has been extensively used in measurements of the wavenumber spectrum, and dissipation and other turbulence measures requiring spatial gradients of field properties like velocity, temperature, concentration, etc.

Following Champagne (1978), let us consider that the velocity field $\mathbf{u}(\mathbf{x},t)$ in a stationary frame is $\mathbf{u}^*(\mathbf{x}^*,t)$ in a frame convected downstream with a velocity U. Then,

$$x_i^* = x_i - Ut\delta_{1i}, \quad u_i^*(\mathbf{x}^*,t) = u_i(\mathbf{x},t) - U\delta_{1i}; \tag{1}$$

$$\left.\frac{\partial u_i(\mathbf{x},t)}{\partial t}\right|_{\mathbf{x}} = \frac{\partial u_i^*}{\partial x_j}\frac{\partial x_j^*}{\partial t} + \frac{\partial u_i^*}{\partial t} = -U\frac{\partial u_i^*}{\partial x_1} + \frac{\partial u_i^*}{\partial t}. \tag{2}$$

If U is sufficiently large and the time rate of change in the convected frame is sufficiently small, it follows that,

$$\frac{\partial}{\partial x_1} = -\frac{1}{U}\frac{\partial}{\partial t}, \tag{3}$$

which is the popular form of the Taylor hypothesis.

Lin (1953) estimated the different terms in the Navier–Stokes equation and derived (3) for large R_λ and low turbulence intensities. By invoking local isotropy at large R_λ, Heskestad (1965) derived an expression relating spatial derivatives of velocity to corresponding temporal derivatives, which allowed correction for large turbulence intensities. Fisher & Davies (1964) showed that large excursions from the mean velocity produce large departures of the convection velocity from the local mean velocity, and explained physical mechanisms which make direct correspondence between true spatial scales and measured temporal scales difficult. The observations of Fisher & Davies prompted Lumley (1965) to analyse different mechanisms that might invalidate the Taylor hypothesis. He showed that at the small scales, all other effects excepting that of a fluctuating convection velocity can be neglected and accordingly proposed a correction model for spectra. Champagne (1978) obtained an analytical solution for the true spectrum on the basis of the Lumley correction, but found that the measured spectrum near the Kolmogorov frequency can exceed the true spectrum by 238 %. Taylor hypothesis has also been found to produce large distortions in the spectra of lateral velocity and scalar fluctuations (Wyngaard & Clifford 1977), and in the probability density functions of velocity and temperature derivatives (Antonia, Chambers & Phan-Thien 1980).

When large-scale motions are considered, the objection to the Taylor hypothesis should be conceptually apparent from the associated large shear and fluctuation intensities. For the case of a pure shear flow $U(y)$, equation (3) suggests that only the first two terms in the x-component of the Navier–Stokes equation,

$$\frac{\partial u}{\partial t} + U\frac{\partial u}{\partial x} + v\frac{dU}{dy} + u_j\frac{\partial u}{\partial x_j} = -\frac{1}{\rho}\frac{\partial p}{\partial x} + \nu\frac{\partial^2 u}{\partial x_j \partial x_j}, \tag{4}$$

are important. The third term is obviously not negligible unless $U\,\partial u/\partial x \gg v\,dU/dy$, i.e. $kU \gg dU/dy$ (Lin 1953); where k is the wavenumber. Thus, for the shear layer at $x/D \simeq 1\cdot5$ in the circular jet discussed in this paper, the hypothesis may be expected to apply for frequency components $f \gg 200$ Hz, whereas the frequency of the large-scale structure studied is 35 Hz. On the other hand, the large-scale structure occurring most frequently in the same jet without excitation (i.e. the preferred mode) is expected to be at 24 Hz. Thus, use of the Taylor hypothesis for studying typical large-scale structures is expected to be grossly in error.

Yet, the Taylor hypothesis has been widely used in situations involving energetic large-eddy motion and in particular, for eduction of large-scale coherent structures (for example, Browand & Wiedman 1976; Yule 1978; Wygnanski & Champagne 1973; Wygnanski, Sokolov & Friedman 1976; Zilberman, Wygnanski & Kaplan 1977; Cantwell, Coles & Dimotakis 1978; Sokolov *et al.* 1980). In many other papers, use of the hypothesis is implicit because structure characteristics are inferred from time traces obtained with stationary sensors. In these kinds of studies, the error introduced by the Taylor hypothesis has been typically assumed non-negligible but never evaluated. This study quantitatively evaluates this error by comparing the 'spatial' distributions of phase-average flow properties obtained via the hypothesis with the measured *actual* spatial distributions.

This experiment was done in a flow involving vortex pairing occurring at a specified location at regular intervals under an appropriate excitation condition. [Additional details are available in Zaman & Hussain (1980) and Hussain & Zaman (1980), hereinafter referred to as I and II, respectively.] A pair of structures during the pairing, and the single structures preceding and at two successive locations following the pairing, in the same flow, provided a variety of structures for which the Taylor hypothesis has been examined. These data thus provide adequate bases for determining the applicability of the hypothesis to turbulent shear flows in general.

2. Experimental procedure

The experiments were carried out in a 7·62 cm diameter air jet discharging into a large laboratory through the centre of a 31-cm end plate, at $Re_D = 3{\cdot}2\times 10^4$. The jet was excited at $St_D(\equiv f_p D/U_e) = 0{\cdot}85$, via a loudspeaker attached to the settling chamber, at an exit amplitude (u_e'/U_e) of 3 %; f_p is the excitation frequency, U_e is the exit velocity, u_e' is the r.m.s. longitudinal velocity fluctuation at $x = 0$, and D is the diameter. For both excited and unexcited situations, the exit boundary layer was laminar and the exit flow was checked to be axisymmetric. Additional details of the apparatus were given in I and Zaman (1978). Measurements were carried out with 4 μ diameter tungsten (single and crossed) hot-wires operated by standard DISA constant temperature anemometers, linearizers, etc.

The jet near-field coherent structures at a single phase are shown schematically in figure 1. The flow field is divided into four measurement 'regions', I–IV. The phase chosen was such that the two pairing toroidal vortices were roughly in their 'radial configuration' in region II. At this selected phase, region I contained a single vortex shortly after its roll-up and regions III and IV captured the merged structure at two successive stages of evolution. In each region, measurements were carried out in two steps. In the first step, actual spatial distributions of the phase-average flow properties were obtained. A reference (single-wire) probe placed in the flow gave the reference ($\tilde{u}$) signal periodic at $\frac{1}{2}f_p$. At a particular phase of this reference signal, selected via a triggering device, data were sampled from the measurement x-wire probe by the on-line laboratory minicomputer (HP2100S). The x-probe was moved to different grid locations by an automated backlash-free traversing mechanism operated by the computer. At each grid point, the averages were computed with a sufficiently large ensemble of data in order to ensure convergence.

In the second step of data acquisition, the probe was traversed in y only, at an x-station in the middle of each measurement region. At each y, the instantaneous $\tilde{u}(t)$

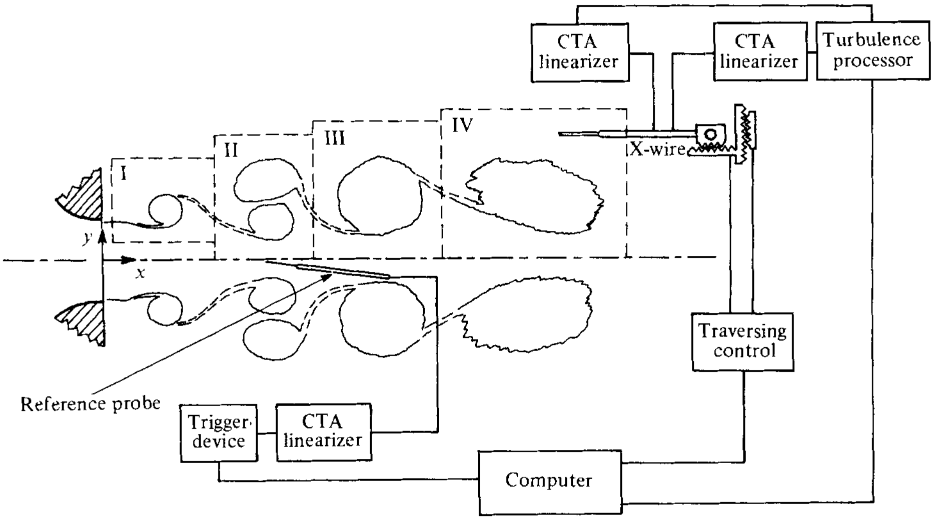

FIGURE 1. Schematic diagram of the flow and probe arrangement.

and $\tilde{v}(t)$ signals were recorded on digital magnetic tapes. Beginning with each trigger, the signals were recorded for a period of time such that the structure 'footprint' was centred in this period. This thus provided data in the (t, y) plane. Each realization consisted of 64 data points spanning about 1·5 times the period of the subharmonic. The ensemble sizes at each y for regions I, II, III and IV were chosen to be 1600, 2880, 3840 and 5760, respectively, in order to satisfy acceptable convergence. The number of y steps used for both stages of data acquisition, i.e. in the (x, y) and (t, y) planes, was the same for each region.

The effect of the Taylor hypothesis on the distributions of the phase-average azimuthal vorticity $\Omega(\equiv \partial\langle v\rangle/\partial x - \partial\langle u\rangle/\partial y)$, where $\langle u\rangle$ and $\langle v\rangle$ are phase averages of $\tilde{u}$ and $\tilde{v}$ (i.e. $\langle u\rangle = \langle\tilde{u}\rangle$), constitutes the principal thrust of our discussion in this paper. Note that deduction of spatial distributions $\Omega(x, y)$ from the time traces of $\tilde{u}$ and $\tilde{v}$ requires use of the Taylor hypothesis twice: first, in conversion of $\partial\langle v\rangle/\partial t$ to $\partial\langle v\rangle/\partial x$ in order to obtain Ω at each (t, y) and then to transform the Ω distribution from the (t, y) plane to the physical plane (x, y). Since the conversion of data from the (t, y) plane to the (x, y) plane is intuitively more perceptible, we concentrate primarily on the subtle aspect of the Taylor hypothesis needed to obtain $\partial\langle v\rangle/\partial x$ from $\partial\langle v\rangle/\partial t$ at each (t, y). Thus we shall mostly focus on $\Omega(t, y)$, i.e. the phase-average of instantaneous vorticity $\tilde{\Omega}$, i.e.

$$\tilde{\Omega}(t,y) = -\frac{\partial\tilde{u}(t,y)}{\partial y} - \frac{1}{U_T}\frac{\partial\tilde{v}(t,y)}{\partial t}, \quad \Omega = \langle\tilde{\Omega}\rangle, \tag{5}$$

where U_T is the convection velocity used in the Taylor hypothesis.

Most of the $\Omega(t, y)$ data will be presented in the (t, y) plane over a typical range of $0 < \tau < 36$ ms. Since this range exceeds the period (28·5 ms) of the structure passage (i.e. the subharmonic), clearly the contour patterns would be expected to repeat at the ends of the τ range. Detailed inspection should reveal small differences between the repeated parts because at increasing times from trigger, the increasing loss of phase reference (i.e. jitter) progressively smears out the contours.

A number of choices for U_T (equation (5)) are possible, notably,

$$U_T = U(y), \quad U_T = \tilde{u}(t,y), \quad U_T = \langle u \rangle (t,y), \quad U_T = U_c. \qquad (6a, b, c, d)$$

Assumption (6*a*) uses the local time-average velocity U. Although Lin's (1953) analysis suggests that this choice may not be at all appropriate for most turbulent shear flows, it has been almost universally used in conversion of time-spectra to wavenumber spectra and in measurements of dissipation and other measures. Assumption (6*b*) would appear quite reasonable since at any instant it is the instantaneous velocity $\tilde{u}$ with which the fluid moves downstream over the probe. Note that Foss (1978) uses this for the measurement of the 'instantaneous vorticity'. Assumption (6*c*) is a compromise between (6*a*) and (6*b*), in that the phase-average vorticity at a selected phase is related to the phase-average velocity $\langle u \rangle$. Assumption (6*d*) uses the structure overall convection velocity U_c, the velocity of the structure 'centre'. This, of course, would be the correct choice only if the structure were a blob of passive fluid convected downstream with U_c. Note that even on a phase-average basis, the assumptions (6*b, c*) are expected to produce noticeably different results for the same flow, the differences arising from the fact that the second term on the right-hand side in (5) is nonlinear in velocity. It is thus clear that even though (6*a*) is extensively used in turbulent shear flows, alternative assumptions for U_T are possible, and there is no *a priori* basis for deciding on the most appropriate choice.

In addition to vorticity, contours of other measures of the coherent structures were also obtained in the (x, y) and the (t, y) planes. These included $\langle u_r^2 \rangle^{\frac{1}{2}}$, $\langle v_r^2 \rangle^{\frac{1}{2}}$, $\langle u_p v_p \rangle$ and $\langle u_r v_r \rangle$, as well as different terms in the equations for the phase-average vorticity and strain rate. The definition of these quantities follow from the triple decomposition, $\tilde{g} = \bar{g} + g_p + g_r$, where g_p is the phase-average contribution due to the coherent structure and g_r is due to the background turbulence field. In order to conserve space, only a limited few of these measurements will be discussed in this paper. Further details of these results can be obtained from the authors.

3. Results and discussion

3.1. *The actual vorticity contours*

The spatial distributions of the phase-average vorticity Ω, computed from measured distributions of $\langle u \rangle (x, y)$ and $\langle v \rangle (x, y)$, are shown in figures 2(*a*)–(*d*) for regions I–IV, respectively. These do not involve use of the Taylor hypothesis, and thus represent the *actual* vorticity distributions within the experimental uncertainty. Note that these data, for the same flow condition and approximate phase as those reported in II, were retaken together with the (t, y) plane data to be discussed later, in order to ensure that the flow conditions were exactly the same for the two data sets.

Figure 2(*a*) shows a type 2 vortex (one which is decelerating and expanding in its toroid diameter prior to pairing, type 1 being the 'leapfrogging' one); figure 2(*b*) shows the two vortices in the 'radial configuration' during pairing; and figures 2(*c, d*) show the paired structure at two successive downstream locations – all at a fixed phase. The low-speed side distortion (i.e. dip) in the vorticity contours is more prominent in the upstream regions. This distortion is due to the combined effects of: (*a*) measurement errors during flow-reversal, i.e. the hot-wires being insensitive to flow direction, and (*b*) jitter in the triggering signal relative to the vortex arrival times, the

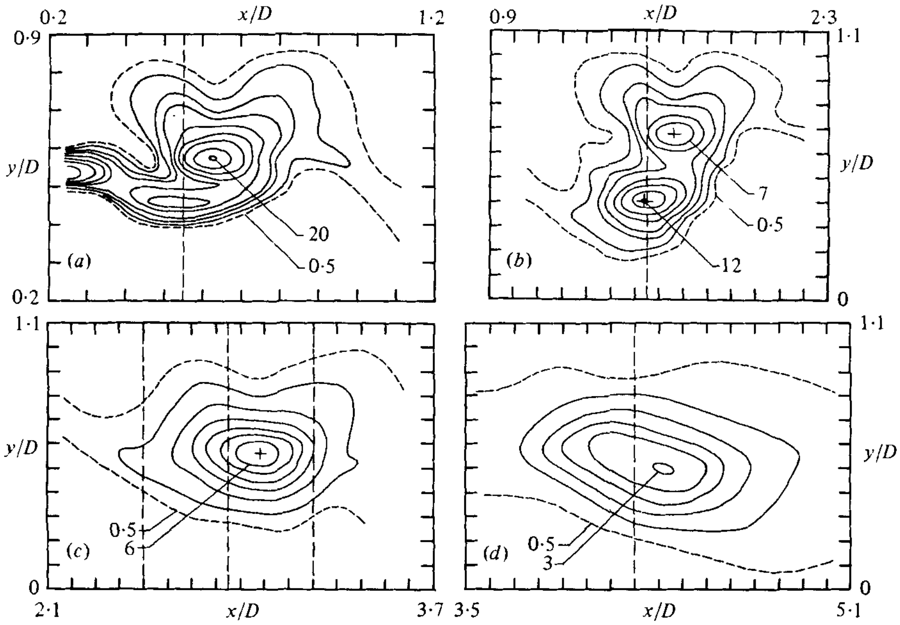

FIGURE 2. Actual spatial distributions of Ω/f_p for the four regions. (*a*) Region I; contour levels are: 20, 15, 10, 7, 5, 3, 2, 1, 0·5. (*b*) Region II; contour levels are: 12, 10, 7, 5, 3, 2, 1, 0·5. (*c*) Region III; contour levels are: 6, 5, 4, 3, 2, 1, 0·5. (*d*) Region IV; contour levels are: 3, 2·5, 2, 1·5, 1, 0·5. Measurements at $Re_D = 3{\cdot}2 \times 10^4$ in a 7·62 cm diameter jet excited at $St_D = 0{\cdot}85$ with $u_e'/U_e = 3\,\%$. Vertical dotted lines represent stations where (t, y) data are taken.

former effect being the more dominant one (further discussed in the next section). The axial locations where the (t, y) plane data were taken in each region are shown as dotted lines in figure 2. Note that for region III, three sets of the temporal data were taken in order to test the sensitivity of the choice of x-station (discussed later). Also note that the $\Omega/f_p = 0{\cdot}5$ contour is shown as a dotted line in this paper because of larger uncertainty at this low vorticity level.

3.2. *Vorticity contours using Taylor hypothesis*

Distributions of $\Omega(t, y)$ were calculated from the measured $\tilde{u}(t, y)$ and $\tilde{v}(t, y)$ by equation (5) using the four choices of U_T (equation (6)). The $\Omega(t, y)$ contours for region I are shown in figure 3; equations 6(*a*)–(*d*) are used for the data in figures 3(*a*)–(*d*), respectively. The data are shown for $-36\text{ ms} < \tau < 0$; the period corresponding to $\frac{1}{2}f_p$ (35 Hz) is 28·5 ms. Since region I is upstream of the pairing location, the passage frequency of the vortices is still f_p, and the chosen time span (in figure 3) captured the vortex pair which later on would coalesce. The vortex on the left in each of figures 3(*a*)–(*d*) is the type 2 vortex (shown in figure 2*a*); the vortex on the right is the type 1 vortex which catches up with the leading vortex and passes through its interior before pairing. It is evident that although both the vortices are still in the process of roll-up, they have already started to attain different characteristics; this is evident from the slightly different cross-sections of the two.

A structure convection velocity of $0{\cdot}4U_e$ has been used in the conversion of $\partial\tilde{v}/\partial t$ to $\partial\tilde{v}/\partial x$ in figure 3(*d*), this being the convection velocity of vortex 2 at this location; for details see I. It is evident that while the other three choices of U_T produce large

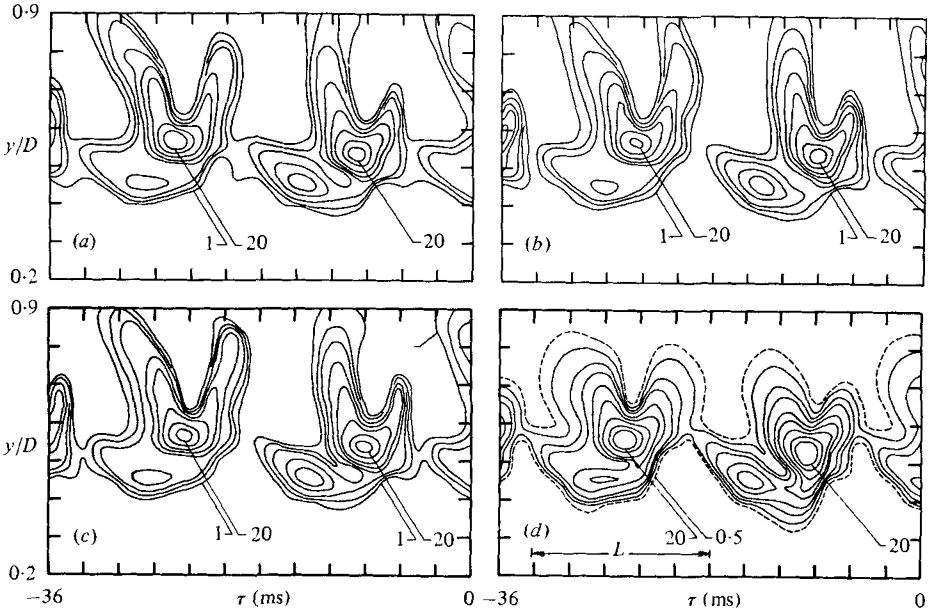

FIGURE 3. $\Omega(t, y)/f_p$ for region I. Conversion schemes used are: (*a*) $U_T = U(y)$, (*b*) $U_T = \tilde{u}(t, y)$, (*c*) $U_T = \langle u \rangle (t, y)$ and (*d*) $U_T = U_c (= 0{\cdot}4U_e)$. Unmarked contour levels in sequence are: 15, 10, 7, 5, 3, 2 and 1.

distortions in the Ω contours in figures 3 (*a*)–(*c*), use of the structure convection velocity as a constant value for U_T produces a structure shape quite close to the actual shape shown in figure 2 (*a*). In fact, if the abscissa is converted to x ($= U_c \tau$), the longitudinal extent of vortex 2 ($L \simeq 0{\cdot}5D$) agrees quite well with that of the vortex in figure 2 (*a*); note that the agreement of the overall transverse extent is also excellent. The schemes in figures 3 (*a*)–(*c*), i.e. use of the local time-average, instantaneous and phase-average velocities produce distributions somewhat similar to one another, but all are distinctly different from the actual. Note that the low-speed side distortion in these cases is especially aggravated.

In the *actual* vorticity contours, the occurrence of the 'dip' on the low-speed side was explained in II. The effect of the sign error in hot-wire measurement of u at instants of flow-reversal is to introduce an error in the $\partial \langle u \rangle / \partial y$ term, although v and thus $\partial \langle v \rangle / \partial x$ are measured correctly. This error in $\partial \langle u \rangle / \partial y$ results in a shift of the Ω contours towards the jet centre-line, thus creating the 'dip'. In the three conversion schemes in figures 3 (*a*)–(*c*), an error is also introduced in the $\partial \langle v \rangle / \partial x$ term at the locations that involve flow-reversal. This is in addition to the error in the $\partial \langle u \rangle / \partial y$ term and occurs because $\partial \langle v \rangle / \partial t$ (measured without the sign error) is divided by U_T (which has sign error at instants of flow-reversal). This produces a cumulative aggravation of the 'dip', which is further accentuated by the fact that U_T values at these locations are small (for equations 6*a*–*c*), thus exaggerating the error due to the term $(1/U_T)\, \partial \langle v \rangle / \partial t$. In comparison with the actual contours, it is clear that the 'dip' is least in figure 3 (*d*). This is to be expected because no error is introduced by 6 (*d*) in the $\partial \langle v \rangle / \partial x$ term since $\partial \langle v \rangle / \partial t$ is divided by a constant positive velocity (U_c) everywhere. No attempt has been made to correct for the flow reversal effect, because it is not apparent that a practical scheme can be developed to correct for this measurement error inherent to hot-wires.

Vorticity distributions $\Omega(t,y)$ for region II, using equations 6(*a*)–(*d*), are shown in figures 4(*a*)–(*d*), respectively. The corresponding distributions for regions III and IV are shown in figures 5(*a*)–(*d*) and 6(*a*)–(*d*), respectively. Region II contains the two vortices during most intense pairing activity. The two here have widely different convection velocities, $1{\cdot}25U_e$ for vortex 1 (inner) and $0{\cdot}35U_e$ for vortex 2 (outer). Figure 4(*d*) shows the structures educed by using an average of the two velocities, namely $U_T = 0{\cdot}8U_e$; the structure shapes educed by using the individual convection velocities will be discussed later. Note that the time axis in figures 4(*a*)–(*d*) have been reduced to $-30 < \tau < 0$. It is evident that the shapes and sizes of the structures in figures 4(*a*)–(*d*) are distinctly different from the actual shape and size shown in figure 2(*b*). This is not unexpected in view of the rapid change and relative motion of the two vortices in this region.

The region III captures a single vortical structure after the completion of pairing. The schemes (*a*)–(*d*) of equation (6) produce quite similar cross-sections, except in figure 5(*d*) where the transverse extent is lesser, agreeing better with the actual distribution in figure 2(*c*). However, large differences remain between each of these distributions and the actual. Especially, note the 'protrusion' in the front high-speed end of the structure and the 'kink' in the contours; these are not present in figure 2(*c*). The protrusion is due to the remnant of vortex 1 and it is evident that, when viewed in time with a probe located at $x/D = 2{\cdot}85$, the merger of the two vortices was not quite completed; clearly, the contour details will depend on the choice of the x-station also (discussed later).

All four of equations 6(*a*)–(*d*) educe quite similar vorticity distributions in region IV, as shown in figures 6(*a*)–(*d*), each agreeing well with the actual distributions shown in figure 2(*d*). This region contains a structure after the completion of pairing and thus is relatively 'passive', and any of the schemes is fairly successful in educing the structure cross-section. The more pronounced sensitivity of the contours to the Taylor hypothesis in region III is to be expected, because when viewed in time from a point within this region, the individual identities of the two vortices have not been lost yet. As we have seen in region II, the Taylor hypothesis then would not be expected to work well.

The above results suggest a pattern. For a single structure, Taylor hypothesis works quite well when used with the constant structure convection velocity. In the case when the structure is passive, the contours in the (t,y) plane are even insensitive to the specific choice of U_T. When the structure is undergoing rapid changes, especially during interactions like tearing or pairing, the hypothesis introduces large distortions. In this case, an average structure passage velocity used as the convection velocity makes the use of the hypothesis least objectionable. In order of increasing passivity, we rank the regions II, III, I, IV, respectively. Thus, the hypothesis works best in region IV and worst in region II.

All the vorticity contours in figures 3–6 are shown in the (t,y) plane. Since the purpose of the Taylor hypothesis is to obtain spatial distribution, it is necessary to examine the distortion introduced in the $t \rightarrow x$ transformation. The $\Omega(x,y)$ contours for regions I–IV, obtained from the (t,y) plane data, are shown in figures 7(*a*)–(*d*), respectively. The $U_T = \langle u\rangle(t,y)$ scheme has been used for figures 7(*a*)–(*c*), while $U_T = U(y)$ has

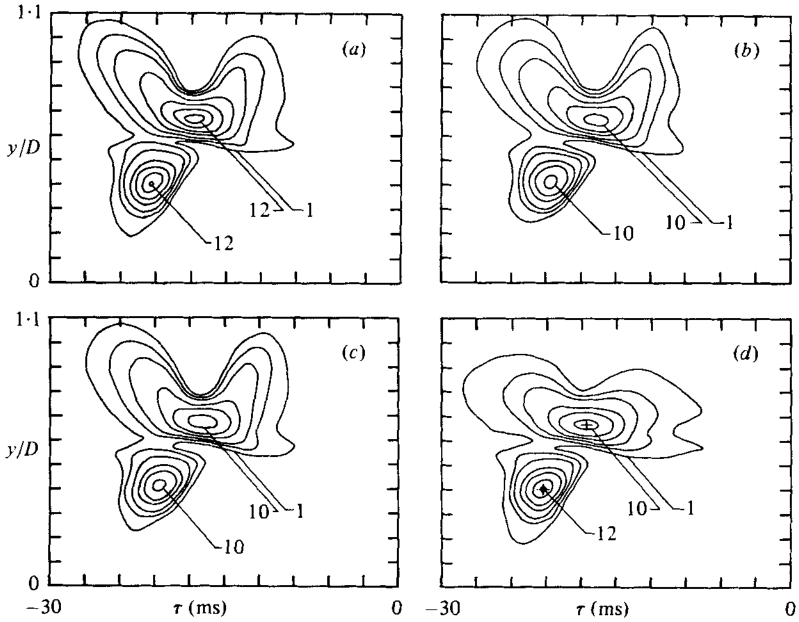

FIGURE 4. $\Omega(t, y)/f_p$ for region II. Conversion schemes used are: (*a*) $U_T = U(y)$, (*b*) $U_T = \tilde{u}(t, y)$, (*c*) $U_T = \langle u \rangle (t, y)$ and (*d*) $U_T = U_c (= 0{\cdot}8U_e)$. Unmarked contour levels in sequence are: 10, 7, 5, 3 and 2.

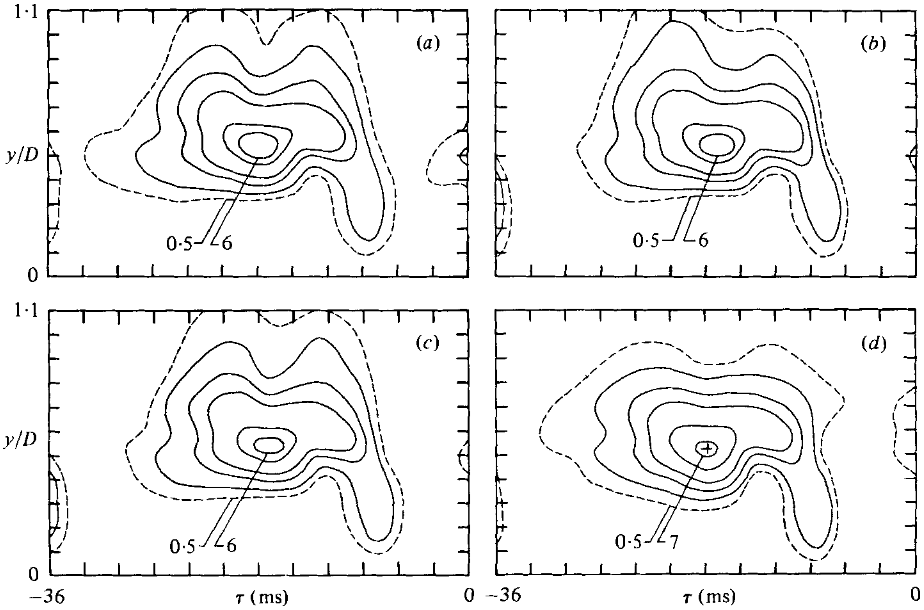

FIGURE 5. $\Omega(t, y)/f_p$ for region III from data taken at $x/D = 2{\cdot}85$. Conversion schemes used are: (*a*) $U_T = U(y)$, (*b*) $U_T = \tilde{u}(t, y)$, (*c*) $U_T = \langle u \rangle (t, y)$ and (*d*) $U_T = U_c (= 0{\cdot}54U_e)$. Unmarked contour levels in sequence are: 5, 3, 2 and 1.

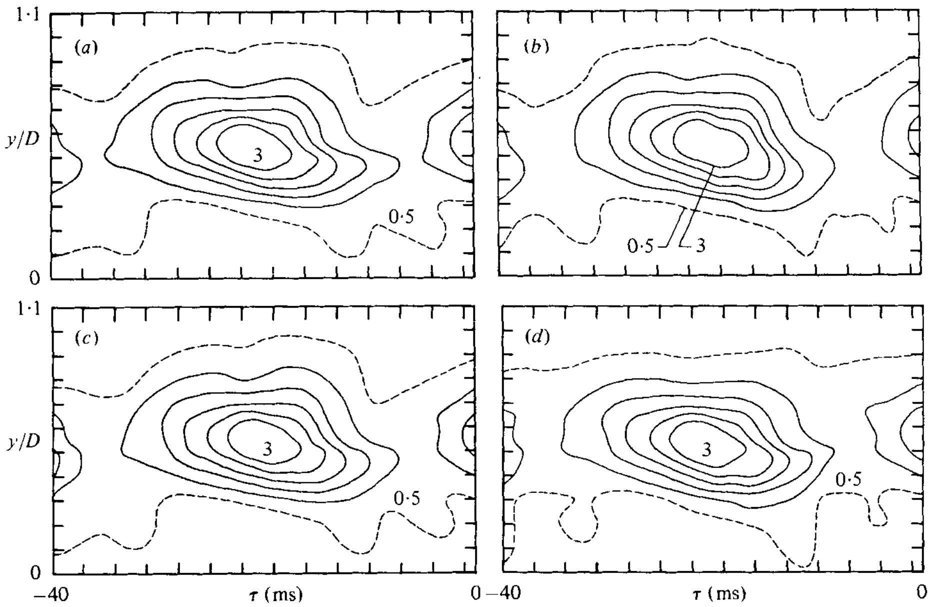

FIGURE 6. $\Omega(t, y)/f_p$ for region IV. Conversion schemes used are: (*a*) $U_T = U(y)$, (*b*) $U_T = \tilde{u}(t, y)$, (*c*) $U_T = \langle u \rangle (t, y)$ and (*d*) $U_T = U_c (= 0{\cdot}58 U_e)$. Unmarked contour levels in sequence are: 2·5, 2, 1·5 and 1.

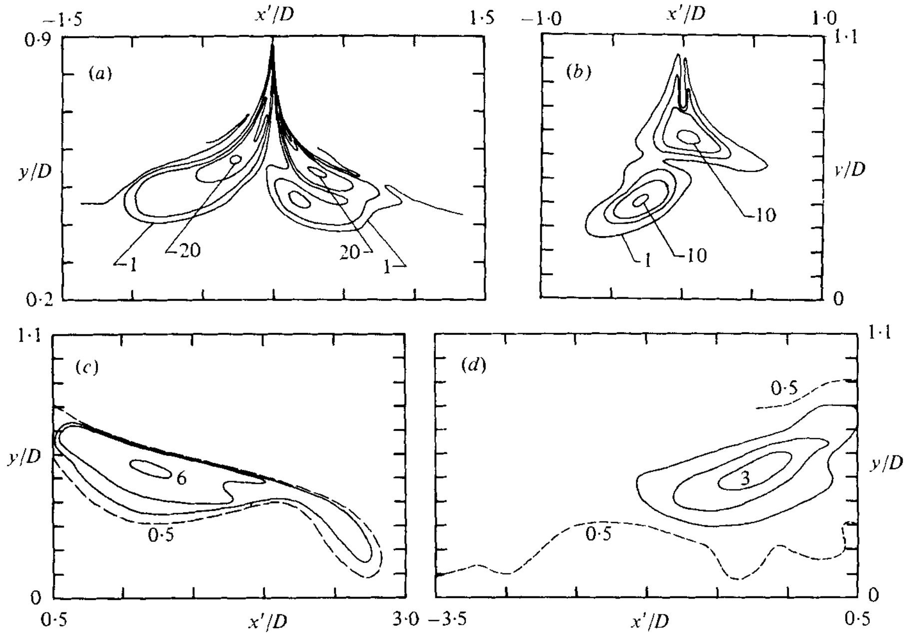

FIGURE 7. $\Omega(x, y)/f_p$ from the (t, y) data. (*a*) Region I; $U_T = \langle u \rangle (t, y)$; contour levels are: 20, 7, 3 and 1. (*b*) Region II; $U_T = \langle u \rangle (t, y)$; contour levels are: 10, 5, 3 and 1. (*c*) Region III; $U_T = \langle u \rangle (t, y)$; contour levels are: 6, 2, 1 and 0·5. (*d*) Region IV; $U_T = U(y)$; contour levels are: 3, 2, 1 and 0·5.

been used for figure 7(*d*) – for the $t \to x$ as well as $\partial v/\partial t \to \partial v/\partial x$ transformations. Note that the origin of the x co-ordinate in each of figures 7(*a*)–(*d*) was assigned to an arbitrary point in time within the structure passage interval, and thus the abscissa in these figures are denoted by x'. Different choices of the time origin will produce different contour shapes from the same data whenever U_T is not a constant across the shear flow. The gross distortion of the contours in each of the figures is evident; this is not unexpected in view of the large gradient in either of $U(y)$ and $\langle u \rangle (y)$ across the shear layer. Note that the relatively lesser, though unacceptably large, distortion in the contours in figure 7(*d*) should not be taken to indicate that $U(y)$ is better than $\langle u \rangle (y)$ as a choice for U_T. This is merely a consequence of the fact that the gradient in $U(y)$ in region IV is less than that in the upstream regions. If $U_T = U(y)$ were used for the $t \to x$ conversion in figure 7(*a*), for example, and the same time origin were assigned to correspond to $x' = 0$, a distribution very similar to that in figure 7(*a*) would result.

It should be emphasized that conversion of $t \to x$ with a constant convection velocity would produce the same contours as shown in figures 3–6. When such conversion is done with the structure average convection velocity, the axial extents of the vortical structures agree quite well with those of the actual vorticity distributions in figure 2, except in region II where there is no unique structure convection velocity. Note further that use of $\tilde{u}(t, y)$ for the $t \to x$ conversion is equivalent to using $\langle u \rangle (t, y)$, and thus are not shown.

The effect of using a single convection velocity in region II is further examined in figure 8; the Ω contours drawn with the convection velocities of vortex 1 ($1{\cdot}25U_e$) and vortex 2 ($0{\cdot}35U_e$) are shown in (*a*) and (*b*), respectively. For comparison, see the corresponding actual spatial distribution in figure 2(*b*), and the distribution using an average convection velocity, i.e. $U_T = 0{\cdot}8U_e$, in figure 4(*d*). It is clear that use of the convection velocity of vortex 1 further distorts vortex 2 (figure 8*a*), and vice versa (figure 8*b*). Thus in region II, the Taylor hypothesis can not produce satisfactory results with any choice of the reference frame velocity. It is clear that similar will be the case in regions and instants of tearing and 'slippage' which appear to be as frequent in turbulent shear flows as pairing is (Hussain & Clark 1981).

The educed structure from the (t, y) plane data can have pronounced dependence on the x-location where the data are taken, because the structure can undergo large evolutionary changes with x. The (t, y)-plane data discussed so far were taken at x-stations where the structures at the selected phase were approximately centred. The effect of the choice of the x-station with respect to the structure is demonstrated in figure 9, where Ω contours are shown for region III. Figures 9(*a*, *b*) correspond to data taken at $x/D = 2{\cdot}5$ and $x/D = 3{\cdot}2$, respectively. Figure 5(*d*) shows the same contours when the data were taken at $x/D = 2{\cdot}85$. The locations of these three stations relative to the structure at the selected phase are indicated in figure 2(*c*).

Figure 9(*a*) shows contours inferred from data at an earlier x-station, and the still ongoing pairing activity is evident. The sequence of structure shapes in figures 9(*a*), 5(*d*) and 9(*b*) agree with visualization observations of the pairing event, in which the inner vortex 1 is actually seen to overtake the slower moving outer one, while the smoke streaks from the former unwind and wrap around the latter. In figure 9(*a*), the protrusion of the vorticity contours and the associated structure in the front is due to vortex 1 while the structure on the left is vortex 2. Figure 9(*b*) shows that even

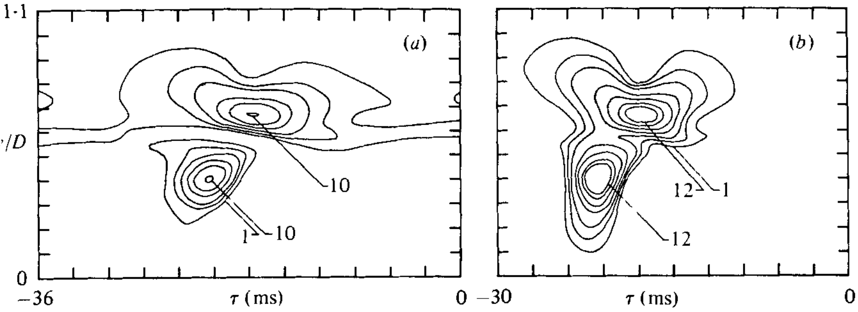

FIGURE 8. $\Omega(t, y)/f_p$ for region II. (a) $U_T = 1{\cdot}25U_e$ (the convection velocity of vortex 1); (b) $U_T = 0{\cdot}35U_e$ (the convection velocity of vortex 2). Unmarked contour levels are in the sequence: 10, 7, 5, 3, 2 and 1.

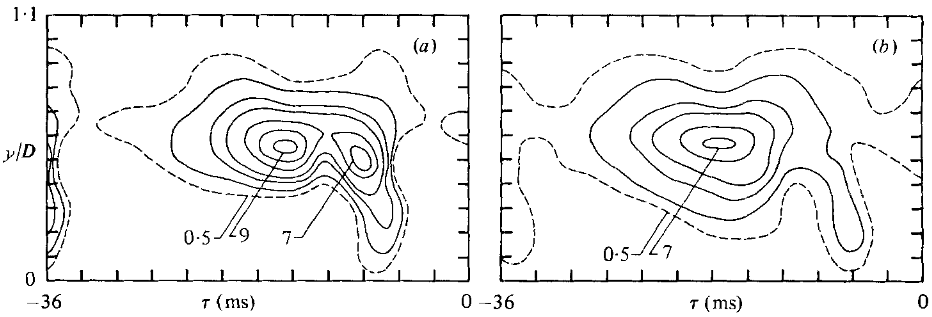

FIGURE 9. $\Omega(t, y)/f_p$ for region III from (t, y) data taken at: (a) $x/D = 2{\cdot}5$, (b) $x/D = 3{\cdot}2$. Unmarked contour levels are in the sequence: 7, 5, 3, 2 and 1.

at $x/D = 3{\cdot}2$, the (t, y) plane data capture remnants of the pairing activity as is clear from the protrusion of the contours in the front, due to vortex 1. But as expected, this protrusion progressively vanishes with increasing downstream shift of the measurement station; for example, compare the $\Omega/f_p = 2$ contours in figures 9(a), 5(d) and 9(b). Note that the 'protrusion' in figure 9(b) is captured by the probe when the structure centre is located farther upstream than that shown in figure 2(c). Clearly, if the (t, y) data were obtained at a station farther downstream, the protrusion would not appear. It is also worth mentioning that from the vorticity peaks in figures 5(d) and 9(b), the time of travel between the two stations separated by $\Delta x = 0{\cdot}35D$ is found to be $\Delta\tau = 8$ ms. This gives a convection velocity $\Delta x/\Delta\tau$ of the merged structure equal to $0{\cdot}54U_e$ agreeing with the data in I.

3.3. *Comparison of phase-average turbulence intensity contours*

While at any (t, y), computation of Ω involves use of the Taylor hypothesis, several other phase-average measures such as the turbulence intensities $\langle u_r^2\rangle^{\frac{1}{2}}$ and $\langle v_r^2\rangle^{\frac{1}{2}}$ can be computed directly. For the $t \rightarrow x$ transformation, these intensity data are presented for regions II and III, as examples. The actual spatial distributions and the (t, y) plane data are shown side by side. For region II, the $\langle u_r^2\rangle^{\frac{1}{2}}$ data are shown in figures 10(a, b) and $\langle v_r^2\rangle^{\frac{1}{2}}$ data in figures 10(c, d), respectively. It is clear that a $t \rightarrow x$ transformation only by a constant convection velocity, equal to the structure passage velocity, would yield spatial distributions resembling the actual distributions. All other values of U_T in (6) would result in gross distortions, similar to those shown in

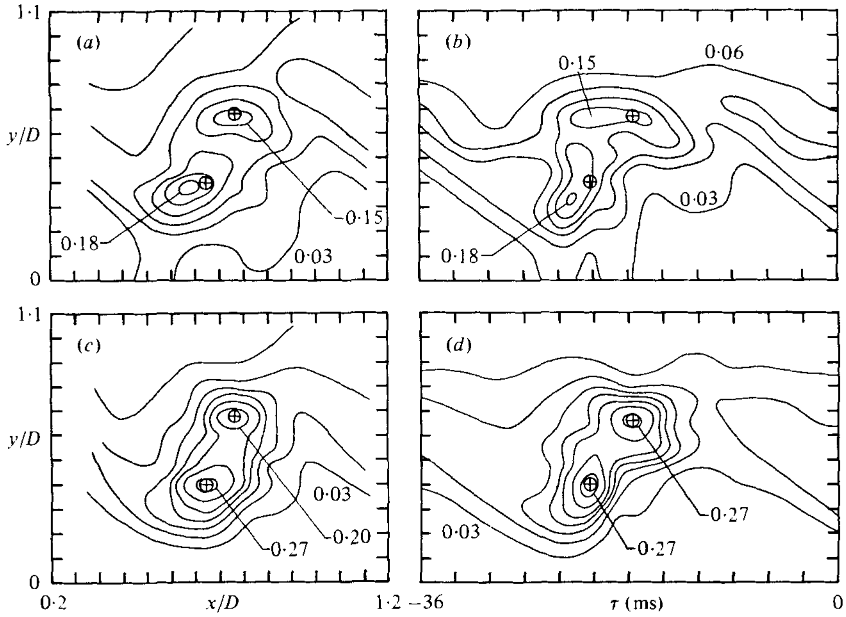

FIGURE 10. Spatial and temporal distributions of phase-average turbulence intensities for region II. (*a*), (*b*) for $\langle u_r^2\rangle^{\frac{1}{2}}/U_e$; contour levels are: 0·18, 0·15, 0·12, 0·09, 0·06 and 0·03. (*c*), (*d*) for $\langle v_r^2\rangle^{\frac{1}{2}}/U_e$; contour levels are: 0·27, 0·20, 0·15, 0·12, 0·09, 0·06 and 0·03.

figures 7(*a*)–(*d*) for vorticity. For region II in figures 10, however, even an average convection velocity of $0{\cdot}80U_e$ used for the $t \rightarrow x$ transformation results in contours with details and streamwise extents differing from the actual.

A similar observation can be made for region III for which, the $\langle u_r^2\rangle^{\frac{1}{2}}$ data are shown in figures 11(*a*, *b*) and $\langle v_r^2\rangle^{\frac{1}{2}}$ data in figures 11(*c*, *d*), respectively, in a similar fashion as in figures 10(*a*)–(*d*). For these data, the longitudinal extents of the spatial distributions obtained from (t, y) plane data, are very close to those of the corresponding actual spatial distributions, if the structure convection velocity of $0{\cdot}54U_e$ is used everywhere across the flow. However, differences continue to exist in the details. The corresponding differences between the same data in the (x, y) and (t, y) planes are of a lesser extent for region IV and relatively more for region I.

The differences in the contours in the (t, y) and (x, y) planes are expected to depend on the particular property considered. The extent of difference should depend on the corresponding time scale involved. The time scale of the coherent structure is much larger than that of the background turbulence. Properties like coherent vorticity Ω are thus expected to undergo minimal distortions within periods of the structure passage while the background turbulence quantities like $\langle u_r^2\rangle^{\frac{1}{2}}$, $\langle v_r^2\rangle^{\frac{1}{2}}$ may undergo considerably larger distortions during the same period. It may thus appear surprising that the background turbulence properties in the (x, y) and (t, y) planes exhibit so close similarities. This can be reconciled by the fact that the background turbulence field and the coherent structure field are not uncoupled; for example, the coherent vorticity Ω can be shown to be linked with the gradients of the background Reynolds stress $\langle u_r v_r\rangle$ (see II). Not only is the dynamics of background turbulence controlled by coherent properties, the turbulence is also embedded in the coherent structure.

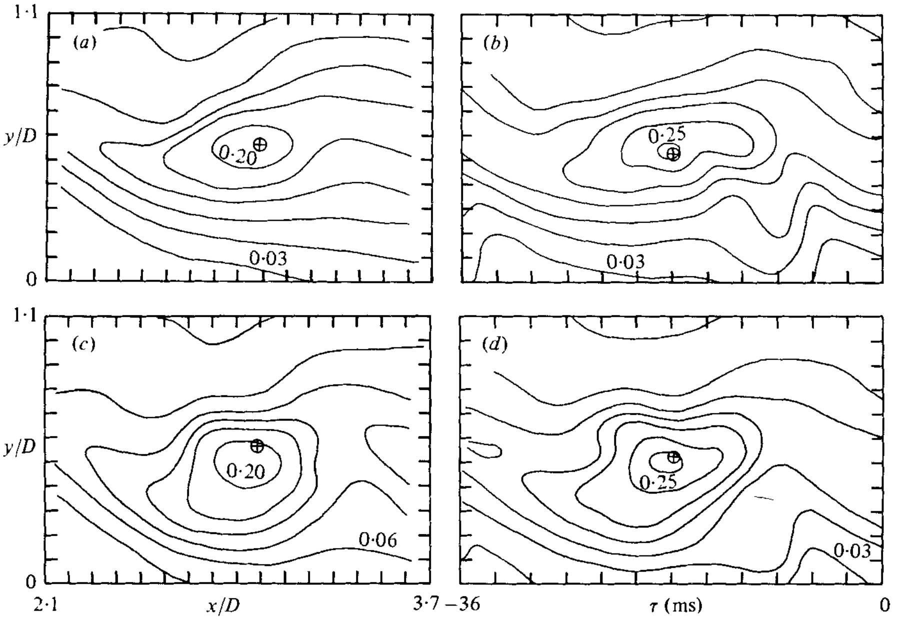

FIGURE 11. Spatial and temporal distributions of phase-average turbulence intensities for region III. (a), (b) for $\langle u_r^2\rangle^{\frac{1}{2}}/U_e$; contour levels are in the sequence: 0·25, 0·20, 0·15, 0·12, 0·09, 0·06 and 0·03. (c), (d) for $\langle v_r^2\rangle^{\frac{1}{2}}/U_e$; contour levels are in the sequence: 0·25, 0·20, 0·15, 0·12, 0·09, 0·06 and 0·03.

It is perhaps worthwhile to note in passing that vorticity Ω is a more appropriate property for structure identification; $\langle u_r^2\rangle^{\frac{1}{2}}$ and $\langle v_r^2\rangle^{\frac{1}{2}}$, sometimes used as markers for structure boundaries (H. Fiedler, private communication) are obviously relatively insensitive to the structure details. For example, the 'protrusion' in the $\Omega(t, y)$ contours in region III (figure 5*d*) is not as clear in the corresponding $\langle u_r^2\rangle^{\frac{1}{2}}$ or $\langle v_r^2\rangle^{\frac{1}{2}}$ contours (figures 11*b*, *d*). Furthermore, we observe that contours based on $\langle u\rangle$ cannot identify the boundary of a free-shear-layer structure (see II; Hussain, Kleis & Sokolov 1980) unlike the case in the boundary layer (Coles & Barker 1975; Cantwell *et al.* 1978; Wygnanski *et al.* 1976; Zilberman *et al.* 1977).

3.4. *Estimates of terms neglected in the Taylor hypothesis*

In an effort to further evaluate the $\partial\langle v\rangle/\partial t \rightarrow \partial\langle v\rangle/\partial x$ conversion schemes, the equation of motion in the coherent structure flow field was considered and the different terms neglected by the Taylor hypothesis were examined. For convenience, here we will use the decomposition,

$$f(x,t) = \langle f\rangle(x,t) + f_r(x,t), \tag{7}$$

where $\langle f\rangle$ is the phase-average (which includes the time-average, i.e. $\langle f\rangle = \bar{f} + \langle f_p\rangle$) and f_r is the part due to the background turbulence field.

Starting with the phase-average of the Navier–Stokes equation, and assuming that the 'pressure' and 'viscous' forces are negligible, and that the flow-field is axisymmetric on the phase-average, the expression for Ω can be found as,

$$\begin{aligned} -\Omega &= \frac{\partial\langle u\rangle}{\partial y} - \frac{\partial\langle v\rangle}{\partial x} \\ &= \frac{\partial\langle u\rangle}{\partial y} + \frac{1}{\langle u\rangle}\frac{\partial\langle v\rangle}{\partial t} + \frac{\langle v\rangle}{\langle u\rangle}\frac{\partial\langle v\rangle}{\partial y} + \frac{1}{\langle u\rangle}\frac{\partial\langle v_r^2\rangle}{\partial y} + \frac{1}{\langle u\rangle}\frac{\partial\langle u_r v_r\rangle}{\partial x}. \end{aligned} \tag{8}$$

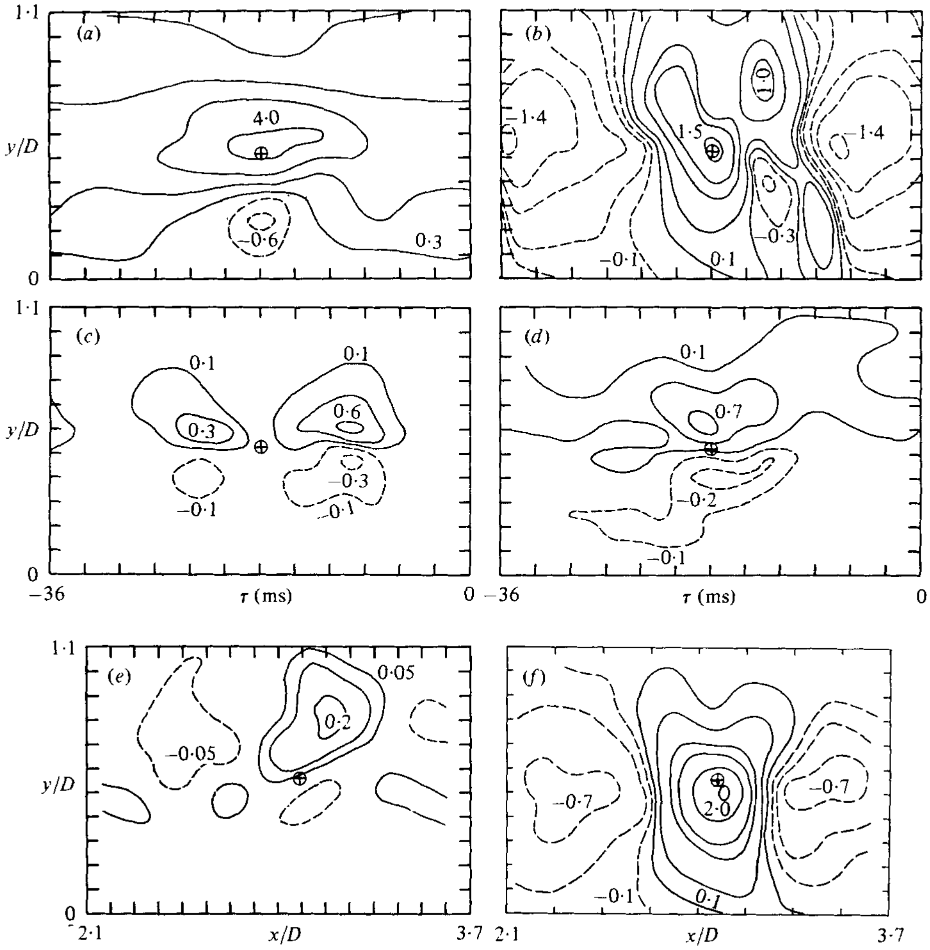

FIGURE 12. Distributions of the different terms in the Ω-equation, non-dimensionalized by f_p.
(*a*) $-\partial\langle u\rangle/\partial y$; contour levels are: 4, 2, 1, 0·3, −0·3, −0·6.
(*b*) $-\langle u\rangle^{-1}\partial\langle v\rangle/\partial t$; contour levels are: 1·5, 1, 0·7, 0·3, 0·1, −0·1, −0·3, −0·7, −1, −1·4.
(*c*) $-(\langle v\rangle/\langle u\rangle)\,\partial\langle v\rangle/\partial y$; contour levels are: 0·6, 0·3, 0·1, −0·1, −0·3.
(*d*) $-\langle u\rangle^{-1}\partial\langle v_r^2\rangle/\partial y$; contour levels are: 0·7, 0·3, 0·1, −0·1, −0·2.
(*e*) $\langle u\rangle^{-1}\partial\langle u_r v_r\rangle/\partial x$; contour levels are: 0·2, 0·1, 0·05, −0·05.
(*f*) $\partial\langle v\rangle/\partial x$; contour levels are: 2, 1·5, 1, 0·7, 0·3, 0·1, −0·1, −0·3, −0·7.

Note that in figures 3(*c*), 4(*c*), 5(*c*) and 6(*c*), only the first two terms of the right-hand side of (8) were used to compute $\Omega(t, y)$.

Each of the terms on the right-hand side of equation (8) were calculated from the phase-average data. As an example, for region III, the distribution of each of these five terms is shown in figures 12(*a*)–(*e*) and the actual $\partial\langle v\rangle/\partial x$ distribution is shown in figure 12(*f*). It is clear from these data that the terms other than $\partial\langle u\rangle/\partial y$ and $\langle u\rangle^{-1}\,\partial\langle v\rangle/\partial t$, are comparatively smaller in magnitude; especially $\langle u\rangle^{-1}\,\partial\langle u_r v_r\rangle/\partial x$ has quite small magnitudes. It is surprising that the coherent momentum transport $\langle v\rangle\,\partial\langle v\rangle/\partial y$ is comparable to, and even less than, the turbulence transport $\partial\langle v_r^2\rangle/\partial y$. However, neither of these two terms is negligible compared to the primary transport terms associated with $\partial\langle u\rangle/\partial y$ or $\langle u\rangle^{-1}\,\partial\langle v\rangle/\partial t$. Note that the transverse gradient $\partial\langle u\rangle/\partial y$ (figure 12*a*) is considerably larger than the gradient $\partial\langle v\rangle/\partial x$ (figure 12*f*).

Region ...	I	II	III	IV
$\Omega_{\text{peak}}\,(x,y)$	20·9	12·3	6·6	3·1
$\dfrac{\partial\langle u\rangle}{\partial y}\,(t,y)$	15·3, −2·4 (85)	8·4, −1·6 (81)	4·8, −0·7 (83)	3·1, −0·07 (102)
$\dfrac{1}{\langle u\rangle}\dfrac{\partial\langle v\rangle}{\partial t}\,(t,y)$	8·2, −9·5 (84)	3·5, −3·9 (60)	1·6, −1·5 (47)	0·8, −0·6 (47)
$\dfrac{\langle v\rangle}{\langle u\rangle}\dfrac{\partial\langle v\rangle}{\partial y}\,(t,y)$	6·1, −1·8 (38)	2·8, −1·2 (33)	0·8, −0·4 (17)	0·15, −0·06 (7)
$\dfrac{1}{\langle u\rangle}\dfrac{\partial\langle v_r^2\rangle}{\partial y}\,(t,y)$	1·0, −0·2 (6)	2·3, −0·7 (24)	0·8, −0·25 (16)	0·4, −0·1 (15)
$\dfrac{1}{\langle u\rangle}\dfrac{\partial\langle u_r v_r\rangle}{\partial x}\,(x,y)$	0·09, −0·1 (1)	0·15, −0·24 (3)	0·11, −0·26 (6)	0·08, −0·11 (6)
$\dfrac{\partial\langle v\rangle}{\partial x}\,(x,y)$	8·2, −2·8 (53)	4·7, −1·6 (51)	2·0, −0·9 (44)	0·8, −1·0 (55)
$\left.\dfrac{1}{\rho}\dfrac{\partial\langle p\rangle}{\partial y}\right\|_{\max}$	6·4 (31)	3·2 (26)	1·2 (18)	0·5 (17)

TABLE 1. Maximum and minimum values of the different terms in equation (8). All values non-dimensionalized by f_p. Range of variation in each region normalized by Ω_{peak} (%) are shown in parentheses.

Note further that as a result of equation 6(*c*), the actual distribution of the gradient $\partial\langle v\rangle/\partial x$ in figure 12(*f*) is approximated by the distribution in figure 12(*b*).

The computed maximum and minimum values for the different terms of equation (8), for each of regions I–IV, are listed in table 1. Each of the terms is non-dimensionalized by f_p; the numbers in the parentheses are the maximum variations in a region expressed as percentage of the peak value of Ω in that region (i.e. 100 × (maximum − minimum)/Ω_{peak}). A note of caution is in order in that these numbers are not for a point in the (x,y) or the (t,y) plane because peaks of the different quantities occur at different locations. These only give an estimate of the relative magnitudes of the different terms for each measurement region. It is obvious that none of the terms $(\langle v\rangle/\langle u\rangle)\,\partial\langle v\rangle/\partial y$ and $\langle u\rangle^{-1}\,\partial\langle v_r^2\rangle/\partial y$ are negligible for any of the regions. The term $\langle u\rangle^{-1}\,\partial\langle u_r v_r\rangle/\partial x$ can, however, be reasonably neglected in the entire flow studied here.

An estimate was made for the pressure term that was neglected in equation (8). The pressure term would appear on the right-hand side of (8) as $+(\rho\langle u\rangle)^{-1}\,\partial\langle p\rangle/\partial y$. The lowest pressure in the centre of the viscous core of a rectilinear vortex is given by (Eskinazi 1967, p. 413),

$$\frac{p_0-p_c}{\rho}=\left(\frac{\Gamma}{2\pi r_*}\right)^2=v_*^2, \tag{9}$$

where p_0 = ambient pressure, p_c = lowest pressure in the viscous core, Γ = circulation around the vortex, r_* = viscous core radius at maximum tangential velocity, and v_* = tangential velocity at r_*. The first equality for p_c in equation (9) was used to obtain estimates of the minimum pressures in the vortex cores, which was cross-checked with estimates from the second equality of (9). The circulation, Γ, was calculated through line-integration of the phase-average velocities $\langle u\rangle$ and $\langle v\rangle$ about the

Region …	I	II		III	IV
		Vortex 1	Vortex 2		
$\dfrac{\Gamma}{U_e D}$	0·5	0·5	0·5	1·0	1·0
r_* (cm)	1·0	1·25	1·75	2·80	3·70
$\left.\dfrac{1}{f_p \rho\langle u\rangle}\dfrac{\partial\langle p\rangle}{\partial y}\right\|_{\max}$	6·4	3·2	1·16	1·2	0·5

TABLE 2. Estimate of the pressure term in the equation for Ω.

structure cross-sections in each region; r_* and v_* were estimated from the $\langle v_p\rangle(x)$ distributions. It was assumed that,

$$\left.\frac{1}{\rho\langle u\rangle}\frac{\partial p}{\partial y}\right|_{\max} \simeq \frac{1}{0{\cdot}5\rho U_e}\frac{p_0-p_c}{r_*}.$$

Accordingly, the magnitude of the pressure term was estimated for each region and is listed in table 2. The value of $(f_p\rho\langle u\rangle)^{-1}(\partial\langle p\rangle/\partial y)|_{\max}$ for each region, expressed as a percentage of the respective Ω-peak value, is also shown in table 1. It can be inferred that the 'pressure term' in the phase-average equation is not negligible. Thus, it seems unrealistic that the $\partial\langle v\rangle/\partial x(t,y)$ term inferred from experimental data in the (t,y) plane can be very accurate. Since no method is known for measuring $p(t,y)$ accurately, one may do the best in approximating $\partial\langle v\rangle/\partial x$ from $\partial\langle v\rangle/\partial t$ through the simplest conversion, using a single convection velocity everywhere across the flow, i.e. via equation 6(*d*).

4. Conclusions

The present results clearly indicate that application of the Taylor hypothesis can be acceptable when applied to single large-scale structures that are not undergoing rapid evolution or interaction with neighbouring structures. Such non-interacting structures exist in all shear flows between interactions. There are examples of shear flows where structure interactions are essentially absent. For eduction of the spatial distributions of structure properties in these cases, Taylor hypothesis can be used without producing large errors while significantly economizing the measurement efforts. In application of the hypothesis, however, one must use a single convection velocity everywhere across the entire shear flow and equal to the structure passage velocity. Uses of the local time-average, phase-average and instantaneous longitudinal velocities produce unacceptable distortions in the educed structure. During large-scale interactions like pairing, tearing or slippage which is typical of turbulent shear flows, no choice of the convection velocity renders the Taylor hypothesis acceptable. The error is least, though large, when an average convection velocity of the interacting structures is used with the hypothesis.

The distributions of the different terms of the equation of motion, contributing to the phase-average vorticity but neglected by the hypothesis, have been quantitatively evaluated. It is apparent that contribution due to gradients of background Reynolds stress is negligible compared to that due to the gradients of phase-average velocities.

In particular, the contribution due to the coherent structure pressure field is quite dominant and cannot be neglected. Evaluation of the different terms contributing to the phase-average strain-rate (not presented) also show that the contribution from the background turbulence field, rather than the coherent motion field, can be neglected.

Since turbulent shear flows are presumed to be dominated by large-scale coherent structures which are continuously evolving and interacting with each other, use of the Taylor hypothesis should be considered unacceptable, in general. It is clear that the widespread use of the local time-average velocity in shear flows especially in the computation of wavenumber spectrum and eduction of large-scale structures is not acceptable. The plausible improvement by the use of the instantaneous velocity is not a solution either. Use of a single structure convection velocity should be an improvement, but this is also not free from limitation in that the structure convection velocity is neither unique nor easily measurable (Wills 1964; Fisher & Davies 1964; Clark & Hussain 1981, in preparation). In a turbulent shear flow, it appears that use of a single velocity, equal to the average of the velocities across the shear region, is the least objectionable choice for the convection velocity in the Taylor hypothesis.

We are grateful to Dr S. J. Kleis for his helpful discussions during the course of this work. The work was supported by the National Science Foundation under Grant ENG 7822110 and the Office of Naval Research under Grant N00014-76-C-0128.

REFERENCES

ANTONIA, R., CHAMBERS, A. J. & PHAN-THIEN, N. 1980 *J. Fluid Mech.* **100**, 193.

BROWAND, F. K. & WIEDMAN, P. D. 1976 *J. Fluid Mech.* **76**, 127.

CANTWELL, B., COLES, D. & DIMOTAKIS, P. E. 1978 *J. Fluid Mech.* **87**, 641.

CHAMPAGNE, F. H. 1978 *J. Fluid Mech.* **86**, 67.

COLES, D. & BARKER, S. J. 1975 *Turbulent Mixing in Nonreactive and Reacting Flows* (ed. S. N. B. Murthy), p. 285. Plenum.

ESKINAZI, S. 1967 *Vector Mechanics of Fluids and Magnetofluids*. Academic.

FAVRE, A., GAVIGLIO, J. & DUMAS, R. 1952 *Proc. 8th Int. Cong. for Appl. Mech. Istambul*, p. 304.

FISHER, M. J. & DAVIES, P. O. A. L. 1964 *J. Fluid Mech.* **18**, 97.

FOSS, J. F. 1978 *Proc. Dynamic Flow Conf.*, p. 983. DISA.

HESKESTAD, G. 1965 *J. Appl. Mech.* **87**, 735.

HUSSAIN, A. K. M. F. & CLARK, A. R. 1981 *J. Fluid Mech.* **104**, 263.

HUSSAIN, A. K. M. F., KLEIS, S. J. & SOKOLOV, M. 1980 *J. Fluid Mech.* **98**, 97.

HUSSAIN, A. K. M. F. & ZAMAN, K. B. M. Q. 1980 *J. Fluid Mech.* **101**, 493.

LIN, C. C. 1953 *Quart. Appl. Math.* **18**, 295.

LUMLEY, J. L. 1965 *Phys. Fluids* **8**, 1056.

SOKOLOV, M., HUSSAIN, A. K. M. F., KLEIS, S. J. & HUSAIN, Z. D. 1980 *J. Fluid Mech.* **98**, 65.

TAYLOR, G. I. 1938 *Proc. Roy. Soc.* A **164**, 476.

WILLS, J. A. B. 1964 *J. Fluid Mech.* **20**, 417.

WYGNANSKI, I. & CHAMPAGNE, F. H. 1973 *J. Fluid Mech.* **59**, 281.

WYGNANSKI, I., SOKOLOV, M. & FRIEDMAN, D. 1976 *J. Fluid Mech.* **78**, 785.

WYNGAARD, J. C. & CLIFFORD, S. F. 1977 *J. Atmos. Sci.* **34**, 922.

YULE, A. J. 1978 *J. Fluid Mech.* **89**, 413.

ZAMAN, K. B. M. Q. 1978 Ph.D. dissertation, University of Houston.

ZAMAN, K. B. M. Q. & HUSSAIN, A. K. M. F. 1980 *J. Fluid Mech.* **101**, 449.

ZILBERMAN, M., WYGNANSKI, I. & KAPLAN, R. E. 1977 *Phys. Fluids Suppl.* **20**, 258.